Doping strategies for increased oxygen permeability of $CaTiO_3$ based membranes

Jonathan. M. Polfus*, Wen Xing, Martin F. Sunding, Sidsel M. Hanetho, Paul Inge Dahl, Yngve Larring, Marie-Laure Fontaine, Rune Bredesen

SINTEF Materials and Chemistry, Forskningsveien 1, NO-0314 Oslo, Norway

*Contact email: jonathan.polfus@sintef.no

Abstract

Oxygen permeation measurements are performed on dense samples of $CaTi_{0.85}Fe_{0.15}O_{3-\delta}$, $CaTi_{0.75}Fe_{0.15}Mg_{0.05}O_{3-\delta}$ and $CaTi_{0.75}Fe_{0.15}Mn_{0.10}O_{3-\delta}$ in combination with density functional theory (DFT) calculations and X-ray photoelectron spectroscopy (XPS) in order to assess Mg and Mn as dopants for improving the O_2 permeability of $CaTi_{1-x}Fe_xO_{3-\delta}$ based oxygen separation membranes. The oxygen permeation measurements were carried out at temperatures ranging between 700-1000 °C with feed side oxygen partial pressures between 0.01-1 bar. The O_2 permeability was experimentally found to be highest for the Mn doped sample over the whole temperature range, reaching 4.2×10^{-3} ml min^{-1} cm^{-1} at 900 °C and 0.21 bar O_2 in the feed which corresponds to a 40% increase over the Fe-doped sample and similar to reported values for x=0.2. While the O_2 permeability of the Mg doped sample was also higher than the Fe-doped sample, it approached that of the Fe-doped sample above 900 °C. According to the DFT calculations, Mn introduces electronic states within the band gap and will predominately exist in the effectively negative charge state, as indicated by XPS measurements. Mn may therefore improve the ionic and electronic conductivity of CTF based membranes. The results are discussed in terms of the limiting species for ambipolar transport and O_2 permeability, i.e., oxygen vacancies and electronic charge carriers.

Keywords: *dense ceramic oxygen membrane; ambipolar transport; mixed ionic-electronic conduction; $CaTiO_3$; calcium titanate*

1. Introduction

Oxy-fuel combustion shows significant potential for implementation of CO_2 capture within power generation and energy intensive industries [1]. Oxygen production by cryogenic distillation is a well-established, but energy demanding process for which only modest improvements are expected in the coming decades. On the other hand, dense ceramic oxygen separation membrane technology shows promise as being more efficient for oxygen production and integration with CO_2 capture processes [2]. Further reduction in the cost and energy penalty associated with integration of this technology may be achieved through improved oxygen permeation rates of stable membrane materials.

$CaTiO_3$-based perovskite oxides have attracted considerable attention as oxygen permeable membranes in particular due to their chemical and mechanical stability under operating conditions involving high temperature, large oxygen chemical potential gradients and CO_2 containing atmospheres [3,4]. These properties, commonly found as shortcomings of the more oxygen permeable $La_{0.5}Sr_{0.5}CoO_{3-\delta}$ and related Co-containing materials, are crucial for the durability and applicability of oxygen permeable membranes [5–11].

Oxygen permeation through $CaTi_{1-x}Fe_xO_{3-\delta}$ (CTF) membranes, where the lower valent Fe^{3+} cation substitutes Ti^{4+} in $CaTiO_3$ lattice, proceeds due to ambipolar transport of oxide ions and electronic charge carriers [12]. The total conductivity increases with Fe content [13], but the ionic conductivity decreases above x≈0.2 due to ordering of oxygen vacancies and partial transition to brownmillerite $Ca_2Fe_2O_5$ [14–17]. Therefore, the ambipolar conductivity and O_2 permeability of CTF are found to be highest for x≈0.2 [4].

The electronic conductivity of $CaTi_{1-x}Fe_xO_{3-\delta}$ is p-type for $p_{O_2} \gtrsim 1\times10^{-5}$ based on reports for x=0.1 between 450-1200 °C [18] and $0 \geq x \geq 0.5$ at 1000 °C [19,20]. These electrical measurements further show that the conductivity is predominately ionic over a relatively wide p_{O_2} range, and the ambipolar conductivity of $CaTi_{1-x}Fe_xO_{3-\delta}$ may therefore be electronically limited even at high temperature and oxidizing atmospheres, e.g., T>1000 °C and p_{O_2}>0.1 bar.

Improvement of the oxygen permeability of $CaTi_{1-x}Fe_xO_{3-\delta}$ is highly desirable. In the present work we further investigate doping strategies for improving the oxygen permeability of the $CaTi_{1-x}Fe_xO_{3-\delta}$ system by fixing x at 0.15 and substituting additional Mg and Mn on the Ti site. Mg is expected to be fully ionized, i.e., $Mg_{Ti}^{//}$, and the effective acceptor concentration is thereby increased, while the charge state of Mn is uncertain and may vary depending on temperature and p_{O_2}. We present results from O_2 permeation measurements of densely sintered disc samples as function of temperature and feed side p_{O_2}. Furthermore, X-ray photoelectron spectroscopy (XPS) and density functional theory (DFT) calculations are employed to elucidate the nature of the dopants in terms of their preferred charge states and electronic structure, as well as association between $Mg_{Ti}^{//}$ and oxygen vacancies.

2. Theory

The simplified electroneutrality condition for acceptor doped $CaTiO_3$ can be written

$$\left[\mathrm{Acc}^{/}\right] = 2[v_O^{\cdot\cdot}] \tag{1}$$

where $\left[\mathrm{Acc}^{/}\right]$ and $[v_O^{\cdot\cdot}]$ are the concentrations of acceptor dopants and oxygen vacancies, respectively, in Kröger-Vink notation. The relative concentration of $v_O^{\cdot\cdot}$ and electron holes, $h^{\cdot}$, respectively, is governed by the equilibrium with oxygen gas

$$\tfrac{1}{2}O_2(g) + v_O^{\cdot\cdot} = O_O^{\times} + 2h^{\cdot} \tag{2}$$

Accordingly, by combining Eq. 1 and 2, the concentration of $h^{\cdot}$, and thereby the electronic conductivity, σ_e, is proportional to $p_{O_2}^{\frac{1}{4}}$. The resulting effect of p_{O_2} on the oxygen permeability, J_{O_2}, can be evaluated from the Wagner equation [21]

$$J_{O_2} = \frac{RT}{16F^2L}\int_{p_{O_2}^{s}}^{p_{O_2}^{f}} \frac{\sigma_O \sigma_e}{\sigma_O+\sigma_e} d\ln p_{O_2} \quad (3)$$

where $p_{O_2}^{f}$ and $p_{O_2}^{s}$ are p_{O_2} at the feed and sweep side, respectively, σ_O is the oxide ion conductivity and $\frac{\sigma_O\sigma_e}{\sigma_O+\sigma_e}$ is the ambipolar conductivity. L is the membrane thickness and R, T and F have their usual meanings. When J_{O_2} is limited by electronic conductivity ($\sigma_e \ll \sigma_O$) and $\sigma_e \propto p_{O_2}^{\frac{1}{4}}$, integration of Eq. 3 yields $J_{O_2} \propto \left(p_{O_2}^{f}\right)^{\frac{1}{4}} - \left(p_{O_2}^{s}\right)^{\frac{1}{4}}$ [22]. On the other hand, if the electronic conductivity is not limiting and the oxide ion conductivity is given by the concentration of $v_O^{\cdot\cdot}$ which is approximately fixed by the dopant concentration (Eq. 1), the ambipolar conductivity is independent of p_{O_2}. Integration of Eq. 3 then yields $J_{O_2} \propto \log\left(\frac{p_{O_2}^{f}}{p_{O_2}^{s}}\right)$, i.e., J_{O_2} is proportional to the ratio of the oxygen pressures at the feed and permeate sides.

3. Experimental

3.1 Synthesis and characterization

Ceramic powders of $CaTi_{0.85}Fe_{0.15}O_{3-\delta}$, $CaTi_{0.75}Fe_{0.15}Mg_{0.05}O_{3-\delta}$ and $CaTi_{0.75}Fe_{0.15}Mn_{0.10}O_{3-\delta}$, denoted CTF, CTFMg5 and CTFMn10, respectively, were synthesized using a route derived from the Pechini method. Nitrate salts were used as starting agents, citric acid as a complexing agent and ethylene glycol for polymerization. An aqueous titanium citrate solution was prepared by applying titanium isopropoxide (Sigma Aldrich, ≥ 97 %) in water containing dissolved citric acid (Sigma Aldrich, 99 %) at 80-90 °C under rigorous stirring for 2 hours before filtering (S & S, Ashless paper filter blue ribbon, 589³). This solution as well as aqueous solutions of $Ca(NO_3)_2{\cdot}H_2O$, $Fe(NO_3)_3{\cdot}9H_2O$, $Mg(NO_3)_2{\cdot}6H_2O$ and $Mn(NO_3)_2{\cdot}4H_2O$ were standardized by thermal decomposition to the respective oxides (CaO, Fe_2O_3, TiO_2, MgO and Mn_2O_3) at 700-1100 °C for 6 h in ambient air. For each synthesis, the standardized nitrate salt solutions were mixed in stoichiometric ratios at a concentration of 0.00052-0.0014 mol cation/g solution. Additional citric acid was added in a molar ratio (citric acid:cations) of 1.1:1, and after stirring for 30 min, ethylene glycol (Aldrich, 99.8%) was added in a molar ratio of 1:1 with respect to citric acid content. The solutions were heated to 120 °C under stirring for 60 min and further evaporated to form dry polymeric gels. Upon heating to 200-250 °C self-ignition occurred and the gels decomposed in a smoldering process. The smoldering temperature varied for the different compositions. The residual powders were pre-calcined at 400 °C, gently crushed in a mortar before further annealing at 900 °C for 6 h in ambient air. The resulting crystalline powders, and later the sintered samples, were analyzed by X-ray diffraction (XRD) using a Bruker D8 Focus diffractometer with Cu Kα radiation and LynxEye detector. In addition to the perovskite phase, a secondary CaO phase was present after annealing at 900 °C. The annealed powders were pressed into pellets of 21 mm diameter and further sintered in air for 6 hours at 1250 °C for CTFMg5 and 1300 °C for CTF and CTFMn10 to obtain fully densified samples free from CaO. The diffraction data was analyzed using the Rietveld method as implemented in the TOPAS software by Bruker. The samples and surfaces were investigated by XRD and scanning electron microscopy (SEM) after O_2 permeation measurements using a FEI Quanta 200 F.

3.2 Oxygen permeation measurements

The sintered disc samples were gradually polished to a roughness of 6 μm with SiC grinding paper and subsequently to a roughness of 1 μm using diamond paste. The final thicknesses of the samples were 1.0, 1.36 and 0.91mm for CTFMn10, CTFMg5 and CTF, respectively. The samples were sealed to alumina support tubes (∅ = 13-16 mm) in a ProboStat measurement cell (NorECs, Norway) using similarly polished gold O-ring gaskets (made by welding gold wire of ∅ = 1 mm). An alumina spring load assembly provided a force of approx. 45 N on the sample against the gold gasket and alumina support tube during sealing and measurements. Mass flow controllers were utilized to supply O_2/He feed gas mixtures and Ar sweep gas at 50 and 25 ml min^{-1}, respectively. The concentrations of O_2 permeate and He leakage were monitored with a Varian CP-4900 gas chromatograph (GC). A S-type thermocouple was placed in the vicinity of the gold O-ring inside the measurement cell, which was inserted into a vertical tube furnace. A successful seal, as determined by a He leakage below the background He level in the GC, i.e., approx. 5 ppm, was usually obtained by heating to 1000 °C. Oxygen permeation fluxes were measured as function of feed side oxygen partial pressure in the range 10^{-2} to 1 bar at temperatures between 700-1000 °C. For dense ceramic membranes, the O_2 permeability, J_{O_2}, is taken as the thickness normalized O_2 flux at given feed and sweep side conditions with units ml(STP) min^{-1} cm^{-1}.

3.3 X-ray photoelectron spectroscopy

After the O_2 permeation measurements, the CTF and CTFMn10 samples were equilibrated at 900 °C in a vertical tube furnace (ambient air, 19 h) and subsequently quenched by dropping them directly into liquid N_2. As such, the equilibrium oxygen non-stoichiometry and dopant charge states at 900 °C may be retained. The samples were fractured under vacuum in the spectrometer in order to expose fresh surface from the bulk of the material and to avoid surface oxidation. XPS spectra were acquired on an Axis Ultra^{DLD} spectrometer (Kratos Analytical, UK) using monochromatic Alα radiation. The employed acquisition settings allow for an energy resolution of 0.7 eV, as determined by the full width at half maximum of the Ag $3d_{5/2}$ peak of sputter cleaned silver.

4. Computational

The DFT calculations were performed using the projector-augmented wave (PAW) method [23,24] as implemented in VASP [25–27]. The generalized gradient approximation by Perdew, Burke and Ernzerhof [28] (GGA-PBE) and the hybrid functional due to Heyd, Scuseria, and Ernzerhof [29] with a screening factor of 0.2 (HSE) was employed. Hybrid functional calculations – intermixing 25% exact Hartree-Fock exchange – provide a proper description exchange interactions in oxides containing multi-valence transitions metals [30,31]. Geometric optimization of the $CaTiO_3$ *Pbnm* cell was performed with a plane wave cut-off energy of 500 eV, and subsequent defect calculations were performed in 2×2×1 supercells (80 atoms) with fixed lattice parameters and a 400 eV cut-off energy. A 3×3×2 supercell (360 atoms) was also used for GGA-PBE calculations of the interaction between $Mg_{Ti}^{//}$ and $v_O^{\cdot\cdot}$. All atomic positions, cell parameters and shapes were optimized until the residual forces for the relaxed atoms were within 0.05 eV $Å^{-1}$ (0.02 eV Å-1 for GGA-PBE) with an energy convergence of 10^{-6} eV for self-consistency. *k*-point sampling was done according to a 2×2×2 Monkhorst–Pack [32] scheme for both supercell sizes. Initial GGA-PBE calculations showed that the stability of $v_O^{\cdot\cdot}$ is very similar on the 4c and 8d oxygen sites with an energy difference of only 0.04 eV, and only the 8d site was considered further for HSE type calculations.

The Gibbs formation energies of oxygen vacancies and cation acceptor dopants in various charge states were calculated from the total energy difference between the defective and perfect supercells according to

$$\Delta G^{\mathrm{f}}_{\mathrm{defect}} = E^{\mathrm{tot}}_{\mathrm{defect}} - E^{\mathrm{tot}}_{\mathrm{perfect}} + \sum_i \Delta n_i \mu_i + q\mu_{\mathrm{e}} \quad (4)$$

where Δn_i is the number of constituent atoms exchanged upon defect formation, μ_i are the atomic chemical potentials, q is the charge state of the defect and μ_{e} is the Fermi level. The atomic chemical potentials define the environmental conditions and the activity of the metal constituents. The chemical potential of gases is obtained from

$$\mu_i(T, p_i) = \mu_i^{\circ} + k_{\mathrm{B}} T \, ln\left(\frac{p_i}{p^{\circ}}\right) \quad (5)$$

where the temperature dependency of μ_i is obtained from thermochemical tables as described by, e.g., Kuwabara et al. [33] The chemical potential of oxygen is defined from the equilibrium between H_2O and H_2 in order to avoid using the O_2 molecule which is problematic within the GGA [34,35]

$$\mu_{\mathrm{O}} = \mu_{\mathrm{H_2O}} - \mu_{\mathrm{H_2}} \quad (6)$$

For H_2O and H_2, μ_i° is taken as the total energies of the respective molecules and the equilibrium partial pressures, p_i, under given conditions are obtained from thermochemical databases [36]. In order to accommodate doping on the Ti-site, the chemical potentials of Ca and Ti were chosen as Ca-rich, i.e.,

$$\mu_{\mathrm{Ti}} = \mu_{\mathrm{CaTiO_3}} - \mu_{\mathrm{Ca}} - 3\mu_{\mathrm{O}} \quad (7)$$

The chemical potentials of Ca, Mg, Fe and Mn were related to the binary oxides, i.e., CaO and MgO ($Fm\bar{3}m$), Fe_2O_3 ($R\bar{3}c$) and Mn_2O_3 ($Pbca$), according to

$$\mu_{\mathrm{M}} = \frac{1}{x}\mu_{\mathrm{M}_x\mathrm{O}_y} - y\mu_{\mathrm{O}} \quad (8)$$

For the solid phases, we approximate $\mu_i = \mu_i^{\circ} = E_i^{\mathrm{tot}}$.

5. Experimental results

5.1 Synthesis and characterization

The sintered CTF and CTFMn10 samples were found to be single phase by XRD with the *Pbnm* space group. For CTFMg5, XRD revealed the presence of MgO in the sample sintered at 1250 °C, as shown in Figure **1**. A more comprehensive structural investigation of the Ca(Ti, Fe, Mn)$O_{3-\delta}$ system will be included in a separate work.

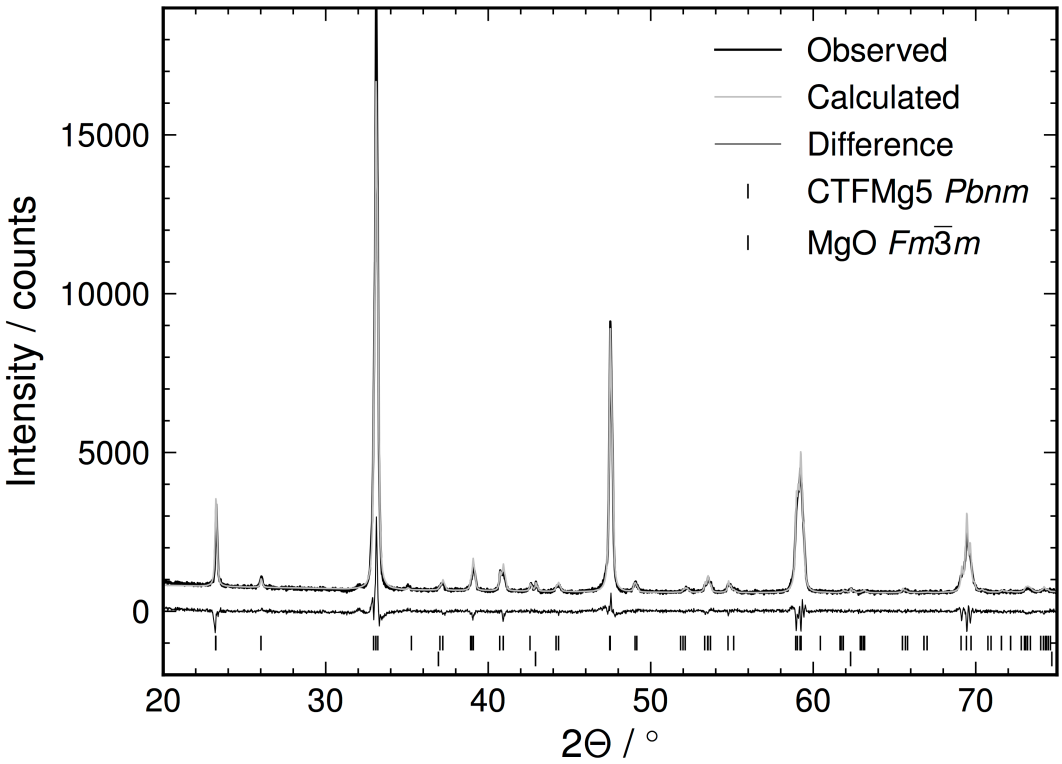

Figure 1: X-ray diffractogram of the CTFMg5 sintered sample showing a secondary phase of MgO. CTFMg5 was fitted to the *Pbnm* space group (a=5.39, b=5.43, c=7.65 Å). The Bragg positions refer to CTFMg5 (top) and MgO (bottom).

XRD and SEM analysis of the samples after O_2 permeation measurements showed no evidence of demixing of the materials during the course of the experiments, as exemplified in the SEM micrograph of the CTFMn10 sweep side surface in Figure 2.

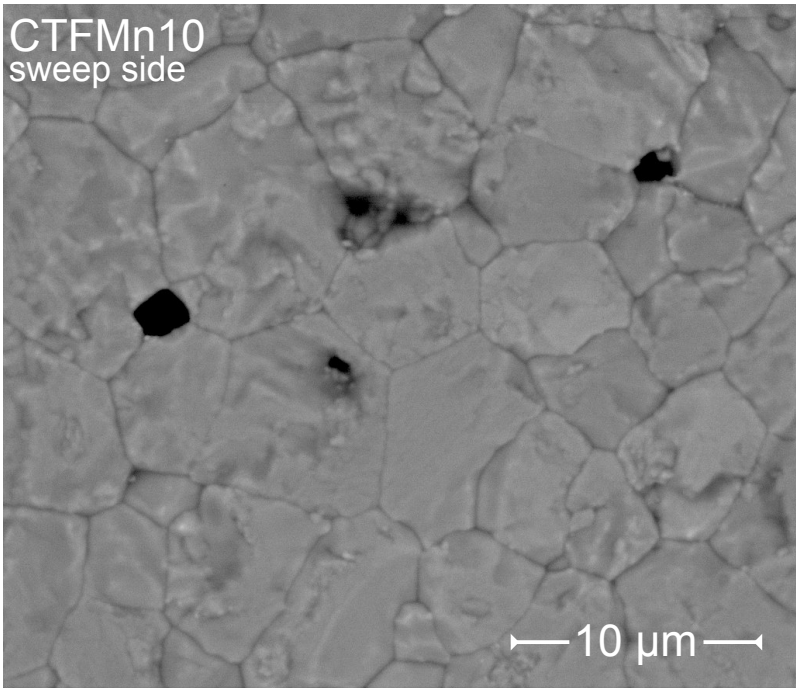

Figure 2: SEM surface micrograph of CTFMn10 sweep side using the backscattered electron detector after permeation measurements for approx. 200 hours.

5.2 O_2 permeation measurements

The oxygen permeabilities, J_{O_2}, of CTFMn10, CTFMg5 and the CTF reference sample are shown as function of inverse temperature in Figure 3a. The O_2 permeability is highest for CTFMn10 at all temperatures, while CTFMg5 is close to CTFMn10 at low temperature and close to CTF at high temperature. Figure 3b shows an Arrhenius type plot of $J_{O_2} \cdot T$ with linear fits in two temperature regimes for all samples. The corresponding activation energies are listed in Table **1**. The CTF sample exhibited a slight lowering of J_{O_2} as function of time at 800 °C with feed side p_{O_2}=0.21 bar (Figure 3), from 1.21 to 1.16×10^{-3} ml min^{-1} cm^{-1} over approx. 18 h. This degradation is significantly lower than that associated with ordering of oxygen vacancies [18,19].

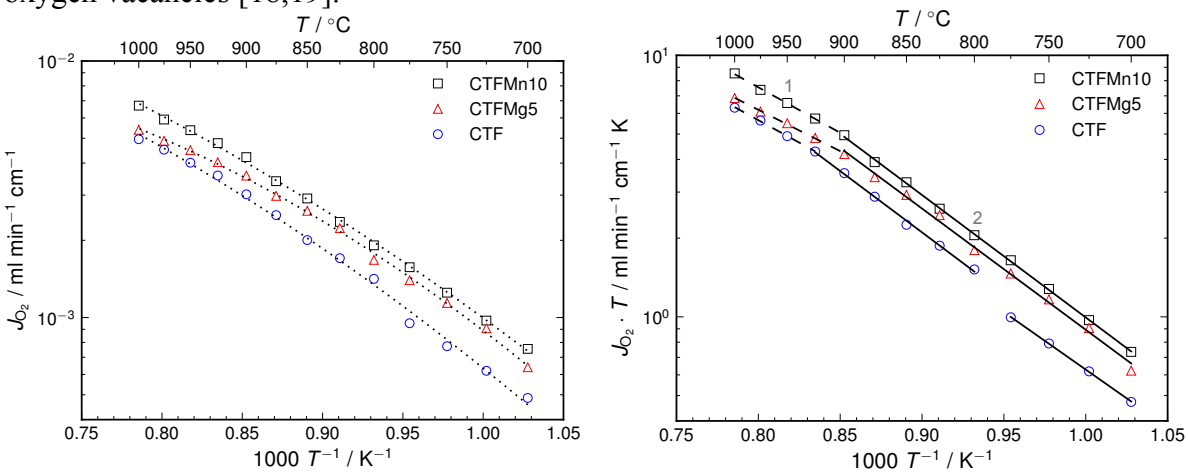

Figure 3: O_2 permeability as function of inverse temperature (a) and Arrhenius type plot with linear fits (b) for feed side p_{O_2}=0.21 bar.

Table 1: Activation energies of O_2 permeability according to the linear fits of the two temperature regions in Figure 3b: 1. high temperature (dashed lines), 2. lower temperature (solid lines).

Specimen	E_a^1 / eV	E_a^2 / eV
CTFMn10	0.69	0.93
CTFMg5	0.63	0.92
CTF	0.68	0.93/0.87

The feed side p_{O_2} dependency of the O_2 permeability is shown for all samples in Figure **4**. At high p_{O_2}, the O_2 permeability is highest for CTFMn10 at all temperatures, while that of CTFMg5 is slightly higher than for CTF except at 900-1000 °C. At p_{O_2}<0.1 bar, the O_2 permeability is highest for CTFMg5 at all temperatures, followed by CTFMn10 and CTF.

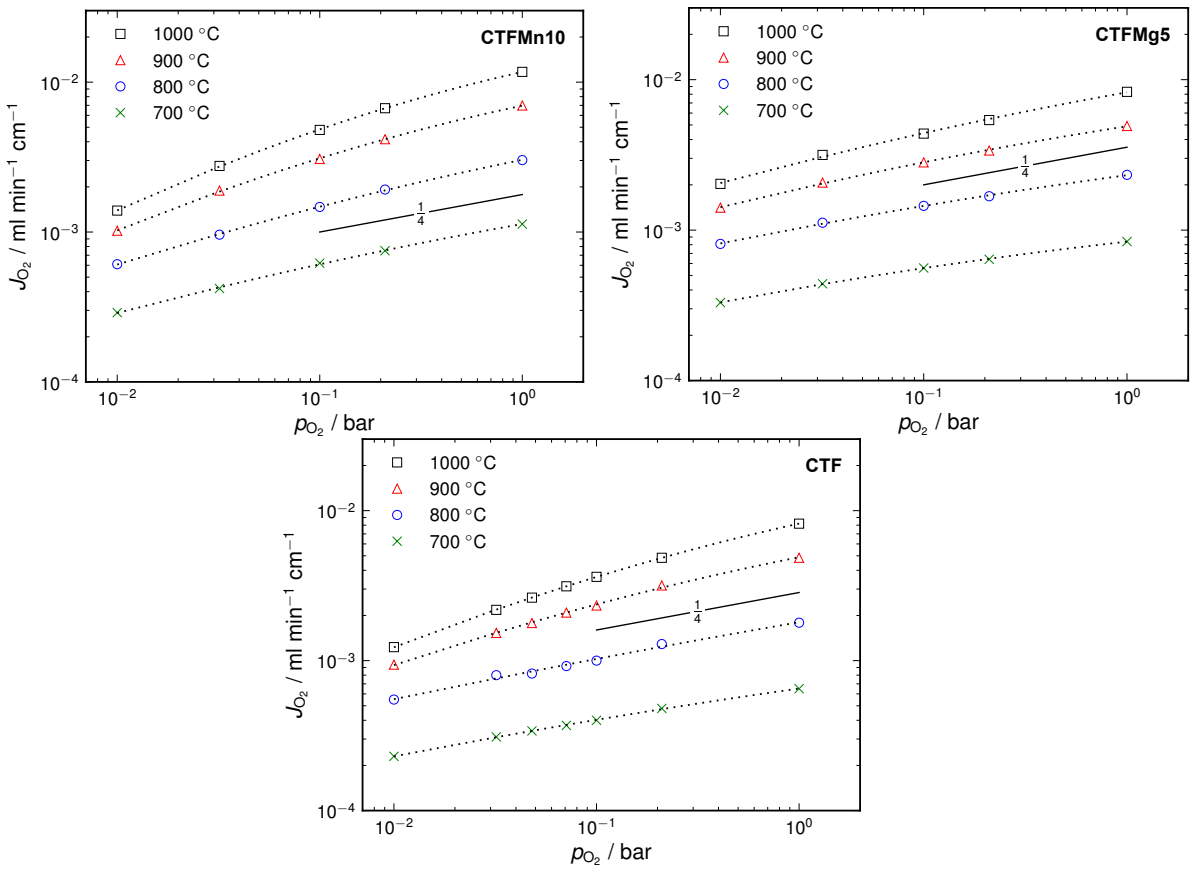

Figure 4: O_2 permeability as function of feed side p_{O_2} at temperatures from 1000-700 °C for CTFMn10 (a), CTFMg5 (b) and CTF (c).

5.3 X-ray photoelectron spectroscopy

Manganese XPS spectra obtained on the CTFMn10 sample are shown in Figure 5, together with Mn 2p reference spectra from Mn_2O_3 and MnO_2 and peak fitting results for Mn 3s. The acquired Mn 2p spectrum fits well with published spectra for Mn_2O_3 (Figure 5a) [37,38], the presence of Mn^{4+} can, however, not be excluded as differences in the bond geometry between MnO_2 and CTFMn10 can lead to differences in the spectral shape. Manganese 3s spectra show a main peak-satellite doublet structure due to multiplet splitting. This spectral structure reflects the total spin of the atom and is thus a good measure of the oxidation state [39]. The separation between the main peak and the satellite amounts to 5.2±0.2 eV in the CTFMn10 sample which indicates an oxidation state near +3 [37,38,40], corresponding to $Mn_{Ti}^{/}$.

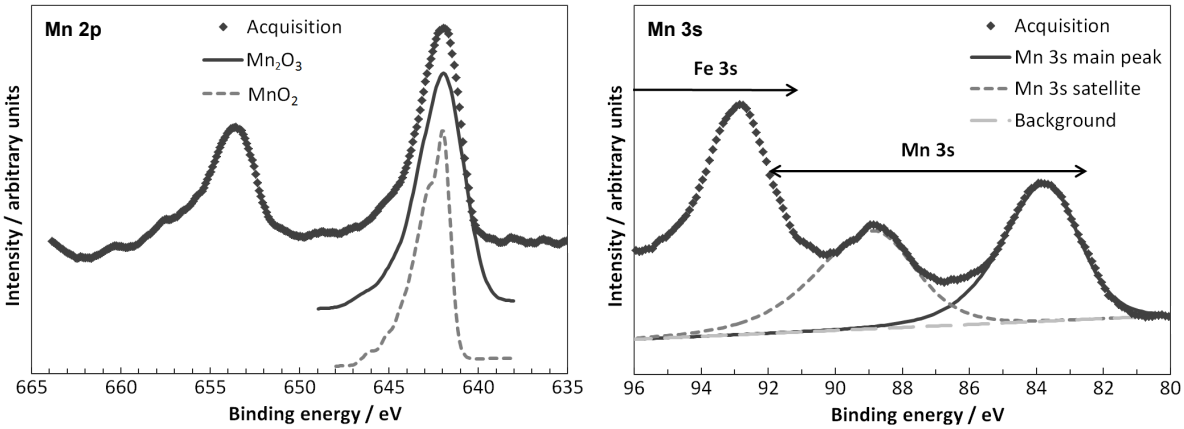

Figure 5: Mn 2p (a) and Mn 3s (b) energy regions for CTFMn10. Reference spectra for Mn_2O_3 and MnO_2 from Biesinger *et al.* [38] are shown in (a) for comparison.

6. Computational results

The Gibbs formation energy of Fe_{Ti}^{q}, Mn_{Ti}^{q}, $Mg_{Ti}^{//}$ and $v_O^{\cdot\cdot}$ is shown as function of the Fermi level at 900 °C and p_{O_2}=0.21 bar in Figure 6. The transition metal dopants, Fe and Mn, may take different charge states. Notably, $Mn_{Ti}^{\times}$ is less stable than the effectively charged counterparts, $Mn_{Ti}^{\cdot}$ and $Mn_{Ti}^{/}$. Furthermore, the thermodynamic transition levels, ε, for Fe and Mn are deep within the band gap and therefore $Fe_{Ti}^{/}$ and $Mn_{Ti}^{/}$ will predominately be charge compensated by $v_O^{\cdot\cdot}$ while electron holes are in minority. Electroneutrality is maintained when ΔG_i^{f} for $v_O^{\cdot\cdot}$ and the cation acceptor dopant is *similar* (the effective charge of the acceptor and site ratio must be considered), as marked with grey circles in Figure 6. Thus, within the dilute limit approximation of these calculations, $Mg_{Ti}^{//}$ is predicted as the most stable acceptor followed by $Fe_{Ti}^{/}$ and $Mn_{Ti}^{/}$, with respect to the binary oxides (see Eq. 8).

The calculations imply that Mn will predominately exist as $Mn_{Ti}^{/}$ in accordance with the results from XPS (section 5.3). Furthermore, a notable amount of Fe may be present as $Fe_{Ti}^{\times}$ due to its rather similar stability to $Fe_{Ti}^{/}$ under these conditions. The latter is in qualitative agreement with the $Fe_{Ti}^{\times}$ concentrations of 2-5% of the total Fe content obtained from Mössbauer spectroscopy [41] and coulometric titration of similar samples [17].

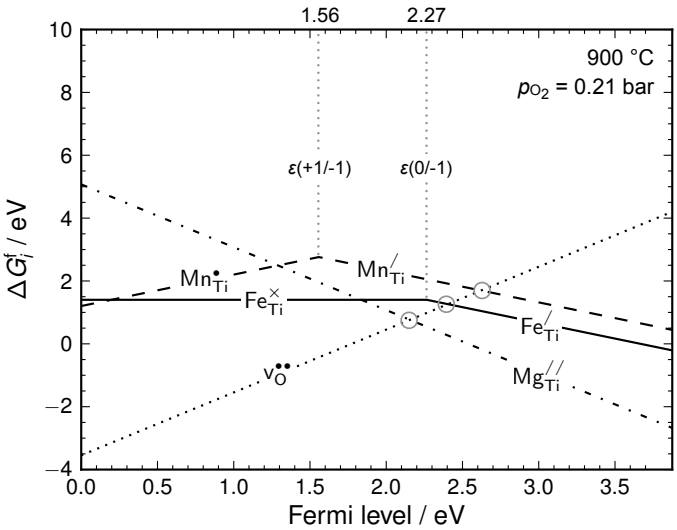

Figure 6: Formation energy of Fe, Mn and Mg on Ti-site in various charge states and fully ionized oxygen vacancies as function of the Fermi level within the theoretical band gap (3.94 eV) at 900 °C and $\boldsymbol{p_{O_2}}$=0.21 bar. The grey circles represent simplified electroneutrality conditions where $\mathbf{v_O^{\cdot\cdot}}$ is predominately charge compensated by $\mathbf{Mg_{Ti}^{//}}$, $\mathbf{Fe_{Ti}^{/}}$, $\mathbf{Mn_{Ti}^{/}}$, respectively.

Figure 7 shows the site-projected electronic density of states for Mg, Mn and Fe in $CaTiO_3$. The valence band is comprised mainly of O-states, while the conduction band is comprised mainly of Ti-states. The occupied Ca and Mg states are located at significantly lower energy (not shown). Fe and Mn introduce electronic states within the band gap corresponding to $Fe_{Ti}^{/}$ and $Mn_{Ti}^{/}$ when filled, consistent with ε(0/-1) and ε(+1/-1), respectively, in Figure 6.

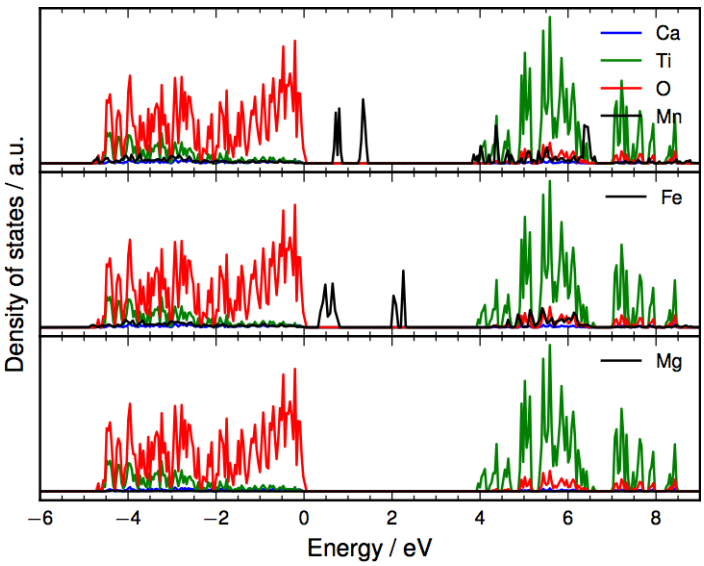

Figure 7: Site projected density of states for $\mathbf{Mn}_{\mathbf{Ti}}^{/}$, $\mathbf{Fe}_{\mathbf{Ti}}^{/}$, $\mathbf{Mg}_{\mathbf{Ti}}^{//}$ and the $CaTiO_3$ constituents. The valence band maximum is referenced to 0 eV.

The binding energy between $Mg_{Ti}^{//}$ and $v_O^{\cdot\cdot}$ was calculated according to association reaction

$$Mg_{Ti}^{//} + v_O^{\cdot\cdot} = (Mg_{Ti}v_O)^{\times} \quad (9)$$

The enthalpy of Reaction 9 was slightly positive, i.e., non-binding: 0.07 and 0.13 eV for the 4c and 8d oxygen site, respectively.

7. Discussion

The general trend in the measured O_2 permeability, which increases in the order CTF<CTFMg5<CTFMn10, may be accounted for by the difference in effective doping concentration: while the nominal amount of $Mg_{Ti}^{//}$ in CTFMg5 is equivalent to that of $Mn_{Ti}^{/}$ in CTFMn10, Mg was not fully dissolved in CTFMg5. The lower solubility of Mg compared to Fe and Mn can be understood from its higher effective charge and in terms of size; the ionic radius of VI-coordinated Mg^{2+}, 0.72 Å, is quite large compared to that of Ti, 0.61 Å, while Fe^{3+} and Mn^{3+} are comparable in size at 0.55-0.65 and 0.58-0.65 Å, respectively [42]. Nevertheless, the role and potential of the Mn, Mg and Fe dopants may be understood from the limiting species for ambipolar transport and O_2 permeability of the different samples.

The O_2 permeability exhibits two rather distinct activation energies within the 700-1000 °C temperature range with a changeover at 900-925 °C (Figure 3b). The low temperature activation energies of 0.87-0.93 eV correspond well with 0.83-0.91 eV reported for ionic conductivity in $CaTi_{1-x}Fe_xO_{3-\delta}$ for $0.2 \geq x \geq 0.1$ [18,19]. At higher temperatures, the ambipolar conductivity and O_2 permeability is increasingly influenced by electronic conductivity. It can be noted that the enthalpy of $h^{\cdot}$ mobility is reported to be in a much lower range, i.e., 0.17-0.23 eV [18,43,44]. The O_2 permeability of CTFMg5 approaches that of CTF in the temperature range where the activation energy is suggested to be increasingly influenced by electronic conductivity. This indicates that $Mg_{Ti}^{//}$ does not contribute to electronic conduction, which can be associated with the lack of electronically active Mg-states (Figure 7). The activation energy of O_2 permeability for CTFMg5 is similar to the other samples and therefore shows no clear evidence of trapping of $v_O^{\cdot\cdot}$ in $(Mg_{Ti}v_O)^{\times}$ complexes in

accordance with the positive binding energies of the nearest neighbor complexes obtained by DFT.

J_{O_2} follows a dependency close to $\left(p_{O_2}^{f}\right)^{\frac{1}{4}}$ for all samples (Figure 4), which is similar to $\left(p_{O_2}^{f}\right)^{\frac{1}{4}} - \left(p_{O_2}^{s}\right)^{\frac{1}{4}}$, indicating that the O_2 permeability is electronically limited as described in Section 2. However, under these feed and sweep side conditions, i.e., $0.01 \leq p_{O_2}^{f} \leq 1$ bar and $1 \times 10^{-4} \leq p_{O_2}^{s} \leq 4.5 \times 10^{-3}$, $\log\left(\frac{p_{O_2}^{f}}{p_{O_2}^{s}}\right)$ corresponds to a similar but slightly lower functional dependency. Thus, the O_2 permeability seems to be in the transition region between being limited by electronic conductivity and being determined by the p_{O_2} gradient.

The O_2 permeability of CTF at 900 °C and $p_{O_2}^{f}$=0.21, 3.0×10^{-3} ml min^{-1} cm^{-1}, is significantly higher than the reported values of 5.2-5.4$\times10^{-4}$ ml min^{-1} cm^{-1}, while that for x=0.2 (CTF20) is higher, 4.0-7.0$\times10^{-3}$ ml min^{-1} cm^{-1}, for various sample thicknesses under similar conditions [45,46]. One may argue that the reported difference in O_2 permeability of more than one order of magnitude is rather surprising considering the slight increase in dopant concentration between CTF15 and CTF20 [45]. CTFMn10 exhibits an O_2 permeability similar to or slightly lower than CTF20 under the same conditions, 4.2×10^{-3} ml min^{-1} cm^{-1}. Still, as being demonstrated in our forthcoming studies, Mn is a promising dopant for improving the O_2 permeability of CTF since it exhibits high dopant solubility without evident ordering of oxygen vacancies [47], and Mn-doped asymmetric tubular membranes exhibit long term stability at 900 °C [48]. The O_2 permeability of CTFMn10 based membranes is however 10-70 times lower than state-of-the-art membrane materials such as $Ba_{0.5}Sr_{0.5}Co_{0.8}Fe_{0.2}O_{3-\delta}$ [5], $Ba_{0.3}Sr_{0.7}FeO_{3-\delta}$ [49], $BaCe_{0.1}Co_{0.4}Fe_{0.5}O_{3-\delta}$ [50], $La_{0.8}Sr_{0.2}Ga_{0.7}Ni_{0.3}O_{3-\delta}$ [51], and $Ce_{0.8}Gd_{0.2}O_{2-\delta}$ with 15 vol% $MnFe_2O_4$ at 900 °C [52]. The superior flux of these membranes may in general be associated with their higher content of multivalent dopants facilitating both ionic and electronic conduction, or the presence of a secondary electronically conducting phase, e.g., $MnFe_2O_4$. In this respect, further improvement of the O_2 permeability of CTFMn10 membranes has been achieved by adjusting the Mn-content [47].

8. Conclusions

Mn is identified as a potential dopant for improving the O_2 permeability of $CaTi_{1-x}Fe_xO_{3-\delta}$ based membranes based on O_2 flux measurements of dense samples of $CaTi_{0.85}Fe_{0.15}O_{3-\delta}$, $CaTi_{0.75}Fe_{0.15}Mg_{0.05}O_{3-\delta}$ and $CaTi_{0.75}Fe_{0.15}Mn_{0.10}O_{3-\delta}$. The O_2 permeability was found to be highest for the Mn-doped sample over the whole temperature range of 700-1000 °C and it was 40% higher than Fe-doped sample at 900 °C and 0.21 bar O_2 in the feed. While the O_2 permeability of the Mg-doped sample was higher than Fe-doped sample, they were quite similar above 950 °C where the O_2 permeability is increasingly governed by electronic conductivity. These findings can be explained by the DFT results: while both Mn and Mg predominately exist in effectively negative charge states, only Mn introduces electronic states within the band gap which may facilitate electronic transport.

9. Acknowledgements

This research has received funding from the European Union Seventh Framework Programme (FP7/2007-2013) via grant agreement no. FP7-ENERGY-268165, “Highly Efficient Tubular Membranes for Oxy-Combustion” (HETMOC). Computational resources were provided through the Norwegian Metacenter for Computational Science (NOTUR) under the project nn9259k.

10. References

[1] IEA, Technology Roadmap: Carbon capture and storage, 2013.

[2] S.S. Hashim, a. R. Mohamed, S. Bhatia, Oxygen separation from air using ceramic-based membrane technology for sustainable fuel production and power generation, Renew. Sustain. Energy Rev. 15 (2011) 1284–1293.

[3] T. Esaka, T. Fujii, K. Suwa, H. Iwahara, Electrical conduction in $CaTi_{1-x}Fe_xO_{3-\delta}$ under low oxygen pressure and its application for hydrogen production, Solid State Ionics. 40-41 (1990) 544–547.

[4] F. Figueiredo, M. Soares, Properties of $CaTi_xFe_xO_3$ ceramic membranes, J. Electroceramics. (2004) 627–636.

[5] Z. Shao, W. Yang, Y. Cong, H. Dong, J. Tong, G. Xiong, Investigation of the permeation behavior and stability of a $Ba_{0.5}Sr_{0.5}Co_{0.8}Fe_{0.2}O_3$ oxygen membrane, J. Memb. Sci. 172 (2000) 177–188.

[6] J. Sunarso, S. Baumann, J.M. Serra, W.A. Meulenberg, S. Liu, Y.S. Lin, et al., Mixed ionic–electronic conducting (MIEC) ceramic-based membranes for oxygen separation, J. Memb. Sci. 320 (2008) 13–41.

[7] S. Baumann, J.M. Serra, M.P. Lobera, S. Escolástico, F. Schulze-Küppers, W. a. Meulenberg, Ultrahigh oxygen permeation flux through supported $Ba_{0.5}Sr_{0.5}Co_{0.8}Fe_{0.2}O_{3-\delta}$ membranes, J. Memb. Sci. 377 (2011) 198–205.

[8] L. Qiu, T.H. Lee, L.-M. Liu, Y.L. Yang, A.J. Jacobsen, Oxygen permeation studies of $SrCo_{0.8}Fe_{0.2}O_{3-\delta}$, Solid State Ionics. 76 (1995) 321–329.

[9] A. Thursfield, I.S. Metcalfe, Air separation using a catalytically modified mixed conducting ceramic hollow fibre membrane module, J. Memb. Sci. 288 (2007) 175–187.

[10] H. Lein, K. Wiik, T. Grande, Kinetic demixing and decomposition of oxygen permeable membranes, Solid State Ionics. 177 (2006) 1587–1590.

[11] P.-M. Geffroy, J. Fouletier, N. Richet, T. Chartier, Rational selection of MIEC materials in energy production processes, Chem. Eng. Sci. 87 (2013) 408–433.

[12] H. Iwahara, T. Esaka, T. Mangahara, Mixed conduction and oxygen permeation in the substituted oxides for $CaTiO_3$, J. Appl. Electrochem. 18 (1988) 173–177.

[13] E. Chinarro, Bulk and grain boundary conductivity of $Ca_{0.97}Ti_{1-x}Fe_xO_{3-\delta}$ materials, Solid State Ionics. 160 (2003) 161–168.

[14] A.I. Becerro, C. McCammon, F. Langenhorst, F. Seifert, R. Angel, Oxygen vacancy ordering in $CaTiO_3$–$CaFeO_{2.5}$ perovskites: From isolated defects to infinite sheets, Phase Transitions. 69 (1999) 133–146.

[15] A. Becerro, F. Seifert, R. Angel, Displacive phase transitions and spontaneous strains in oxygen deficient $CaFe_xTi_{1-x}O_{3-x/2}$ perovskites ($0<x<0.40$), J. Phys. Condens. Matter. 12 (2000) 3661–3670.

[16] C. McCammon, A.I. Becerro, F. Langenhorst, R.J. Angel, S. Marion, F. Seifert, Short-range ordering of oxygen vacancies in $CaFe_xTi_{1-x}O_{3-x/2}$ perovskites ($0<x<0.4$) C, J. Phys. Condens. Matter. 12 (2000).

[17] F.M. Figueiredo, J. Waerenborgh, V. V Kharton, H. Na, J.R. Frade, On the relationships between structure , oxygen stoichiometry and ionic conductivity of $CaTi_{1-x}Fe_xO_3$, Solid State Ionics. 156 (2003) 371–381.

[18] S. Marion, A.I. Becerro, T. Norby, Ionic and electronic conductivity in $CaTi_{0.9}Fe_{0.1}O_{3-\delta}$, Ionics. 5 (1999) 385–392.

[19] L. Dunyushkina, V. Gorbunov, Crystal structure and electrical conductivity correlation in $CaTi_{1-x}Fe_xO_{3-\delta}$ system, Ionics. 8 (2002) 256–261.

[20] L.A. Dunyushkina, V.P. Gorelov, High temperature electrical behavior of $CaTi_{1-x}Fe_xO_{3-\delta}$ ($x = 0–0.5$). Oxygen-ion, electronic and proton conductivity, Solid State Ionics. 253 (2013) 169–174.

[21] P.J. Gellings, H.J. Bouwmeester, Handbook of Solid State Electrochemistry, CRC Press, 1997.

[22] T. Norby, R. Haugsrud, Dense Ceramic Membranes for Hydrogen Separation, in Membranes for Energy Conversion, Wiley-ECH Verlag Gmbh & Co KGaA, 2008.

[23] P.E. Blöchl, Projector augmented-wave method, Phys. Rev. B. 50 (1994) 17953–17979.

[24] G. Kresse, D. Joubert, From ultrasoft pseudopotentials to the projector augmented-wave method, Phys. Rev. B. 59 (1999) 1758–1775.

[25] G. Kresse, J. Hafner, Ab initio molecular dynamics for liquid metals, Phys. Rev. B. 47 (1993) 558–561.

[26] G. Kresse, J. Hafner, Ab initio molecular-dynamics simulation of the liquid-metal-amorphous-semiconductor transition in germanium, Phys. Rev. B. 49 (1994) 14251–14269.

[27] G. Kresse, Efficiency of ab-initio total energy calculations for metals and semiconductors using a plane-wave basis set, Comput. Mater. Sci. 6 (1996) 15–50.

[28] J. Perdew, K. Burke, M. Ernzerhof, Generalized Gradient Approximation Made Simple., Phys. Rev. Lett. 77 (1996) 3865–3868.

[29] J. Heyd, G.E. Scuseria, M. Ernzerhof, Erratum: “Hybrid functionals based on a screened Coulomb potential” [J. Chem. Phys. 118, 8207 (2003)], J. Chem. Phys. 124 (2006) 219906.

[30] T. Archer, C.D. Pemmaraju, S. Sanvito, C. Franchini, J. He, A. Filippetti, et al., Exchange interactions and magnetic phases of transition metal oxides: Benchmarking advanced ab initio methods, Phys. Rev. B. 84 (2011) 115114.

[31] C. Franchini, R. Kovacik, M. Marsman, S.S. Murthy, J. He, C. Ederer, et al., Maximally localized Wannier functions in $LaMnO_3$ within PBE+U, hybrid functionals, and partially self-consistent GW: an efficient route to construct ab-initio tight-binding parameters for e_g perovskites, (2011) 30.

[32] H.J. Monkhorst, J.D. Pack, Special points for Brillouin-zone integrations, Phys. Rev. B. 13 (1976) 5188–5192.

[33] A. Kuwabara, Theoretical investigation to thermal equilibrium concentration of point defect through first-principles calculation, Sci. Technol. Adv. Mater. 8 (2007) 519–523.

[34] I. Batyrev, A. Alavi, M. Finnis, Equilibrium and adhesion of Nb/sapphire: The effect of oxygen partial pressure, Phys. Rev. B. 62 (2000) 4698–4706.

[35] B. Meyer, First-principles study of the polar O-terminated ZnO surface in thermodynamic equilibrium with oxygen and hydrogen, Phys. Rev. B. 69 (2004) 045416.

[36] C.W. Bale, P. Chartrand, S.A. Degterov, G. Eriksson, K. Hack, R. Ben Mahfoud, et al., FactSage thermochemical software and databases, Calphad Comput. Coupling Phase Diagrams Thermochem. 26 (2002) 189–228.

[37] P.A.W. van der Heide, Multiplet splitting patterns exhibited by the first row transition metal oxides in X-ray photoelectron spectroscopy, J. Electron Spectros. Relat. Phenomena. 164 (2008) 8–18.

[38] M.C. Biesinger, B.P. Payne, A.P. Grosvenor, L.W.M. Lau, A.R. Gerson, R.S.C. Smart, Resolving surface chemical states in XPS analysis of first row transition metals, oxides and hydroxides: Cr, Mn, Fe, Co and Ni, Appl. Surf. Sci. 257 (2011) 2717–2730.

[39] D. Briggs, Basic Principles, Spectral Features and Qualitative Analysis, in: D. Briggs, J.T. Grant (Eds.), Surf. Anal. by Auger X-Ray Photoelectron Spectrosc., IM Publications, 2003: pp. 31–56.

[40] V. Di Castro, G. Polzonetti, XPS study of MnO oxidation, J. Electron Spectros. Relat. Phenomena. 48 (1989) 117–123.

[41] J.C. Waerenborgh, F.M. Figueiredo, J.R. Frade, M.T. Colomer, J.R. Jurado, Fe 4+ content and ordering of anion vacancies in partially reduced $AFe_xTi_{1-x}O_{3-y}$ (A = Ca, Sr; $x \leqslant 0.6$) perovskites. An 57 Fe Mössbauer spectroscopy study, J. Phys. Condens. Matter. 13 (2001) 8171–8187.

[42] R.D. Shannon, Revised effective ionic radii and systematic studies of interatomic distances in halides and chalcogenides, Acta Crystallogr. Sect. A. 32 (1976) 751–767.

[43] W.L. George, R.E. Grace, Formation of point defects in calcium titanate, J. Phys. Chem. Solids. 30 (1969) 881–887.

[44] S. Xie, W. Liu, K. Wu, P. Yang, G. Meng, C. Chen, Mixed oxygen ionic and electronic conduction in $CaFe_{0.2}Ti_{0.8}O_{3-\delta}$: a combined oxygen permeation and electrical conductivity study, Solid State Ionics. 118 (1999) 23–28.

[45] F.. Figueiredo, V.. Kharton, a. . Viskup, J.. Frade, Surface enhanced oxygen permeation in $CaTi_{1-x}Fe_xO_{3-\delta}$ ceramic membranes, J. Memb. Sci. 236 (2004) 73–80.

[46] A.L. Shaula, R.O. Fuentes, F.M. Figueiredo, V.V. Kharton, F.M.B. Marques, J.R. Frade, Grain size effects on oxygen permeation in submicrometric $CaTi_{0.8}Fe_{0.2}O_{3-\delta}$ ceramics obtained by mechanical activation, J. Eur. Ceram. Soc. 25 (2005) 2613–2616.

[47] J.M. Polfus, W. Xing, M. Riktor, P.I. Dahl, M.F. Sunding, S.M. Hanetho, et al., Enhanced O_2 Flux of $CaTiO_3$-based membranes by Mn-doping, To Be Submitt. (2015).

[48] W. Xing, M.-L. Fontaine, Y. Larring, J.M. Polfus, Z. Li, P. Henriksen, et al., High temperature $CaTi_{0.6}Fe_{0.15}Mn_{0.25}O_{3-\delta}$ asymmetric tubular membrane fabrication and oxygen flux characterization, To Be Submitt. (2015).

[49] Y. Teraoka, H. Shimokawa, C. Kang, H. Kusaba, K. Sasaki, Fe-based perovskite-type oxides as excellent oxygen-permeable and reduction-tolerant materials, Solid State Ionics. 177 (2006) 2245–2248.

[50] Q. Li, X. Zhu, Y. He, W. Yang, Oxygen permeability and stability of $BaCe_{0.1}Co_{0.4}Fe_{0.5}O_{3-\delta}$ oxygen permeable membrane, Sep. Purif. Technol. 73 (2010) 38–43.

[51] T. Ishihara, T. Yamada, H. Arikawa, Mixed electronic–oxide ionic conductivity and oxygen permeating property of Fe-, Co-or Ni-doped $LaGaO_3$ perovskite oxide, Solid State Ionics. 135 (2000) 631–636.

[52] H. Takamura, K. Okumura, Y. Koshino, a. Kamegawa, M. Okada, Oxygen Permeation Properties of Ceria-Ferrite-Based Composites, J. Electroceramics. 13 (2004) 613–618.